IEEE Photonics Journal
An IEEE Photonics Society Publication

Mapping Surface-Plasmon Polaritons and Cavity Modes in Extraordinary Optical Transmission

Volume 3, Number 3, June 2011

Y. Ding
J. Yoon
M. H. Javed
S. H. Song
R. Magnusson, Senior Member, IEEE

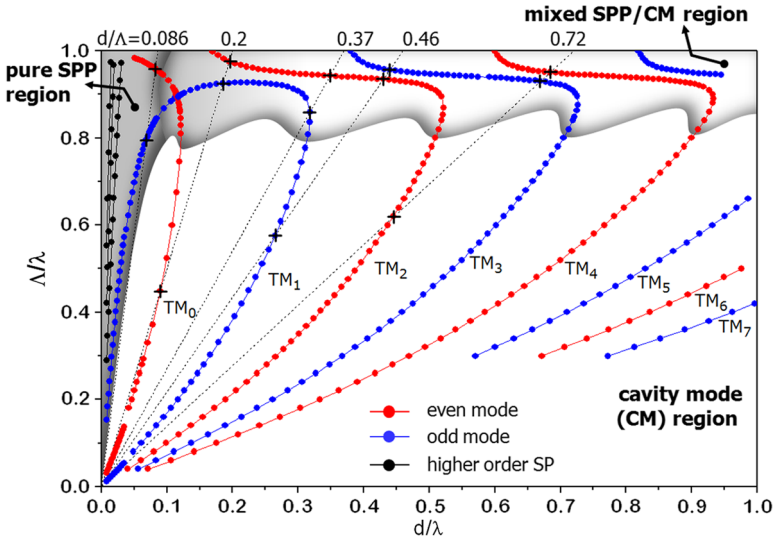

DOI: 10.1109/JPHOT.2011.2138122
1943-0655/$26.00 ©2011 IEEE

Mapping Surface-Plasmon Polaritons and Cavity Modes in Extraordinary Optical Transmission

Y. Ding,[1] J. Yoon,[2] M. H. Javed,[2] S. H. Song,[3] and R. Magnusson,[2] *Senior Member, IEEE*

[1]Resonant Sensors Incorporated, Arlington, TX 76010 USA
[2]Department of Electrical Engineering, University of Texas at Arlington, Arlington, TX 76019 USA
[3]Department of Physics, Hanyang University, Seoul 133-791, Korea

DOI: 10.1109/JPHOT.2011.2138122
1943-0655/$26.00 ©2011 IEEE

Manuscript received March 7, 2011; revised March 25, 2011; accepted March 25, 2011. Date of publication April 5, 2011; date of current version May 6, 2011. This work was supported in part by the UT System Texas Nanoelectronics Research Superiority Award funded by the State of Texas Emerging Technology Fund. Additional support was provided by the Texas Instruments Distinguished University Chair in Nanoelectronics endowment. Corresponding author: R. Magnusson (e-mail: magnusson@uta.edu).

Abstract: Transmission of light through periodic metal films with intensity considerably exceeding that predicted by aperture theory is referred to as extraordinary optical transmission (EOT). The mechanisms responsible for this effect have been investigated intensively during the past decade. Here, we show an elegant method of visualizing the operative physical mechanisms for model resonance systems. By numerically mapping the resonance loci, modal and plasmonic mechanisms emerge clearly with delineated regions of dominance. Thus, the photonic transmission resonances are parametrically correlated with localized electromagnetic fields forming pure surface-plasmon polaritons (SPPs), coexisting plasmonic and cavity-mode (CM) states, and pure CMs. This mapping method renders a consistent picture of the transitions between photonic states in terms of key parameters. It shows how the TM_1 CM seamlessly morphs into the odd SPP mode as the film thickness diminishes. Similarly, the TM_0 mode converts to the even SPP mode. At the intersection of these mode curves, an EOT-free gap forms due to their interaction. On account of a reflection phase shift of a slit-guided mode, an abrupt transition of the resonance loci in the SPP/CM region is observed.

Index Terms: Plasmonics, subwavelength structures, waveguides, gratings, nanocavities, optical properties of photonic materials.

1. Introduction

The coupling of incident electromagnetic waves to localized surface states on patterned films is presently the subject of considerable research activity. Periodic structures with subwavelength features effectively achieve such coupling since zero-order operation can be attained with no higher diffraction orders being present and acting to reduce the strength of the interaction. Associated strong localization of energy at a metallic, mostly opaque surface with corresponding high-amplitude near fields generates extraordinary optical transmission (EOT) [1], [2]. Analogously, on a mostly transparent periodic dielectric layer, high-efficiency reflection can occur at resonance [3].

Discovered over 10 years ago [1], optical transmission through periodic metal films, with levels of intensity well beyond those predicted by the standard aperture theory [4], is referred to as EOT. Occurrence of EOT through 1-D and 2-D periodic structures has been studied intensively. In some papers, surface-plasmon polaritons (SPPs) are found to be chiefly responsible for EOT [1], [5]–[7],

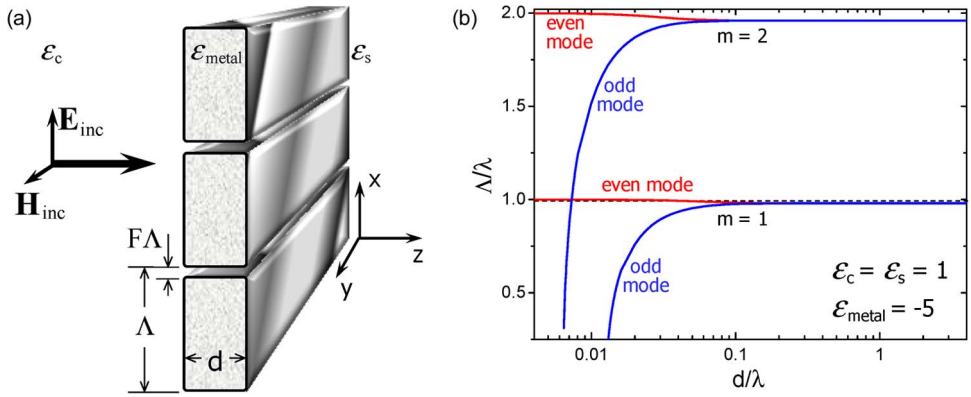

Fig. 1. EOT diffraction problem geometry and dispersion plot. (a) Single-layer 1-D binary metallic grating under TM-polarized incident light with dielectric constants $\varepsilon_c = \varepsilon_s = 1.0$ and $\varepsilon_{metal} = -5.0$. Thickness and modulation period are denoted by d and Λ, respectively. The fill factor (F) of the air gap is the ratio of air gap width and the period. Only normal incidence is studied. (b) Normalized d/λ–Λ/λ plot of a corresponding 1-D binary metallic grating with infinitesimal periodic modulation.

while in others, SPPs deter EOT [8]–[11]. Furthermore, it has been shown that cavity mode (CM) resonances along with SPPs must be considered to fully treat EOT [12]–[15]. Thus, photonic surface modes and CMs have emerged as fundamental causes of EOT. In a recent review paper, Garcia-Vidal *et al.* emphasize the parametric dependence of the operational mechanisms [2]. Mapping this dependence in a normalized parameter space for 1-D slit arrays is the chief goal of the present contribution.

Accordingly, in this paper, we address the resonance properties of metal films possessing periodic slits. The objective of the work is to provide a method of expedient visualization of the operative physical mechanisms in terms of normalized parametric maps. This dispersion plot defines the operating regions of SPP modes and CMs and shows how these regions connect. We limit the study to single-layer structures modulated with 1-D binary profile under normal incidence. The numerical computations are performed using rigorous coupled-wave analysis, assuming transversely infinite structures [16]. We study a canonical case with a real-valued dielectric constant $\varepsilon = -5$ [17], [18] and investigate briefly how the maps change if $\varepsilon = -2$ and $\varepsilon = -10$ are chosen. The model device is shown in Fig. 1(a).

EOT occurs when there is coupling to a discrete photonic state supported by the structure. A common scheme used to elucidate resonance conditions is the wavenumber-frequency $(\beta$–$\omega)$ plot. In this paper, however, the d/λ–Λ/λ (normalized thickness–normalized frequency) plot will be used. The advantage of this approach is that the characteristics of a family of devices are presented compactly and clearly. The classic d/λ–Λ/λ plot of an example metallic waveguide is presented in Fig. 1(b), where we assume an infinitesimal periodic modulation to be present. The plot is prepared based on the dispersion properties of metallic planar waveguides [19], as was the phase-matching relation $\beta = mK$, where β is a propagation constant of a mode, $K = 2\pi/\Lambda$, and m is an integer identifying the diffraction order. Thus, Fig. 1 illustrates the geometry and dispersion map for coupled SPP modes. We note that a part of the higher order-coupled SPP for the odd mode reaches into the zero-order regime where frequency is $\Lambda/\lambda < 1$. A modified version of Fig. 1(b), as pertaining to the metallic diffractive structure under study, will be a main focus point in the remainder of this paper.

2. Results and Discussion

When the modulation of the periodic waveguide increases, its dispersion properties will greatly deviate from what can be estimated from the homogeneous waveguide and phase-matching conditions shown in Fig. 1(b). In this case, we can find the dispersion features by tracking the appearance of EOT peaks in the diffraction spectra. We use this approach to study the physics of the periodic metallic waveguide of Fig. 1(a). Specifically, zero-order transmittance spectra are

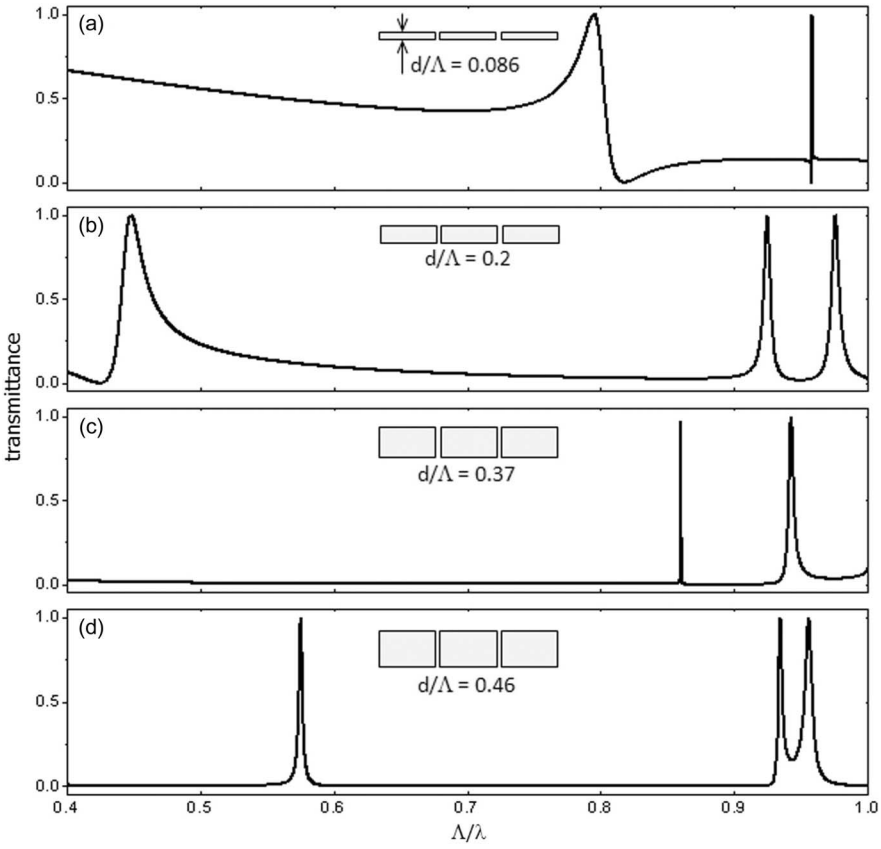

Fig. 2. EOT spectra of a single-layer metallic grating. Grating has fill factor $F = 0.05$ with thickness (a) $d/\Lambda = 0.086$; (b) $d/\Lambda = 0.2$; (c) $d/\Lambda = 0.37$; and (d) $d/\Lambda = 0.46$.

calculated for structures with various thicknesses [20]. Four example spectra are presented in Fig. 2, where $F = 0.05$. Then, the transmission peaks are found and compiled into the normalized d/λ–Λ/λ plot, as in Fig. 3.

In Fig. 3(a), the collection of circular dots represents the resonance loci found through rigorous numerical calculations. As the system is mirror symmetrical, localized modes at EOT resonance have either even or odd symmetry as indicated by red and blue dots, respectively. Each curve is marked by TM_i, with i indicating the number of nodes in the magnetic field pattern inside a slit. Note that only the frequency range with $\Lambda/\lambda < 1$ is presented in Fig. 3(a) so that none of the extraordinary diffraction spots shown is contributed by the Rayleigh condition, i.e., the canonical Wood's anomaly. The resonances for a particular thickness fall on a straight line $(d/\Lambda = \text{constant})$ in Fig. 3, starting from the origin with the inverse slope of the line equal to the normalized thickness. Several such lines are presented in Fig. 3. The resonance peaks associated with these exemplary lines are marked by a cross $(+)$ symbol.

The resonance mechanisms associated with the dispersion map of Fig. 3(a) can be identified by their correlation with the dispersion characteristics of possible localized photonic states, i.e., SPPs and slit-guided (SG) modes. In Fig. 3(b), where the EOT resonance loci are indicated by gray circular symbols, we superimpose dispersion curves for coupled SPPs and Fabry-Pérot (FP) resonances of a fundamental SG mode inside a grating slit [11], [21], [22].

First, the FP-type resonances of a fundamental SG mode (green curves) are obtained by the usual condition given by

$$\beta_{SG} d_q + \phi_R = q\pi \tag{1}$$

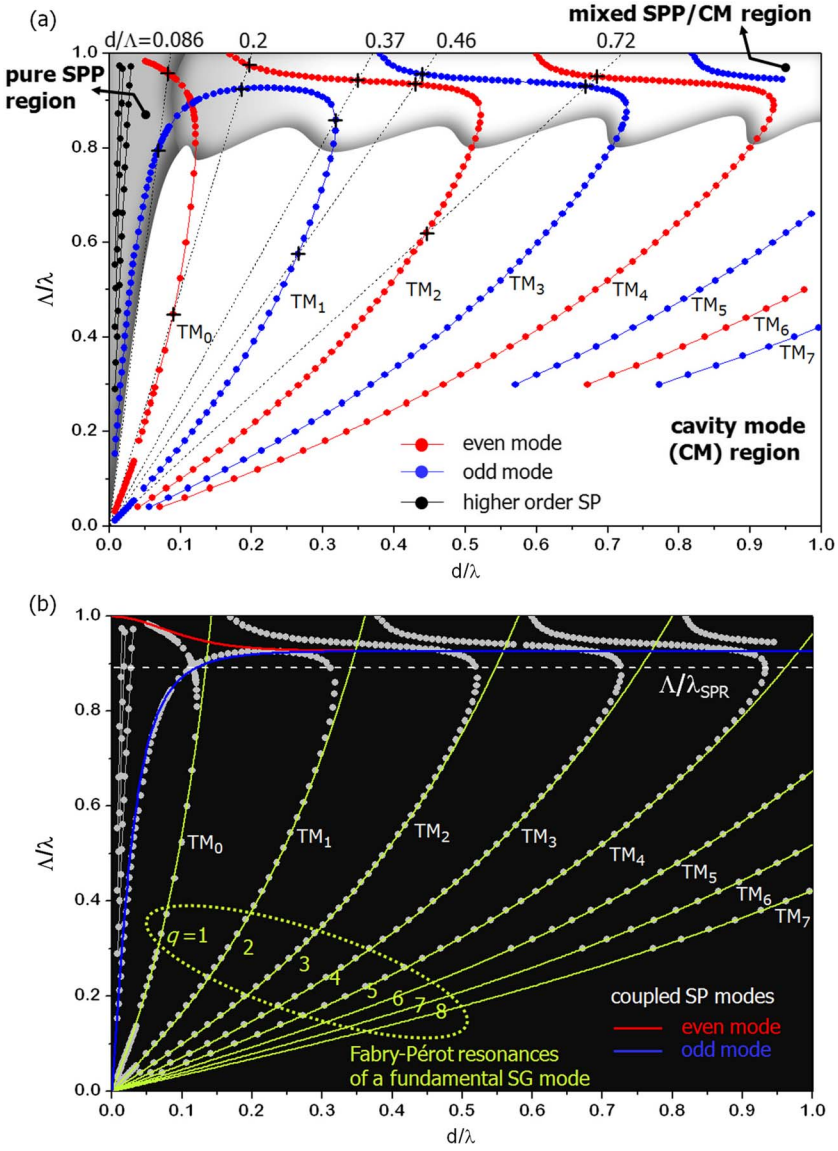

Fig. 3. Parametric EOT maps. (a) d/λ–Λ/λ dispersion map of resonance loci for a single-layer metallic grating with narrow air slits ($F = 0.05$). The mode number (TM_i) indicates the number of zero crossing points in the transverse magnetic field. The plot is divided into three approximate regions according to the operative mechanism, as shown by shading. (b) Overlay of dispersion curves for coupled SPP modes (red and blue curves) on a homogeneous metal film with infinitesimal modulation on the EOT curves. We also overlay Fabry-Pérot resonances (green curves) of a fundamental slit-guided (SG) mode inside an isolated slit. The homogeneous metal film for red and blue curves has $\varepsilon_{\text{eff}} = -7.143$ computed via the mean value of $1/\varepsilon$ in the grating. The dashed horizontal line indicates SP resonance frequency $\Lambda/\lambda_{\text{SPR}}$ on a single metal surface with $\varepsilon_{\text{metal}} = -5$.

where β_{SG} is the propagation constant of a fundamental SG mode propagating along the z-axis inside an isolated slit, ϕ_R is the phase shift associated with reflection of this mode at the slit end facet, and q is an integer. The propagation constant of a fundamental SG mode for a slit width $w = F\Lambda$ is given by the dispersion relation [23]:

$$\tanh\left(\frac{w}{2}\sqrt{\beta_{\text{SG}}^2 - k_0^2}\right) = -\frac{1}{\varepsilon_{\text{metal}}}\sqrt{\frac{\beta_{\text{SG}}^2 - \varepsilon_{\text{metal}} k_0^2}{\beta_{\text{SG}}^2 - k_0^2}} \tag{2}$$

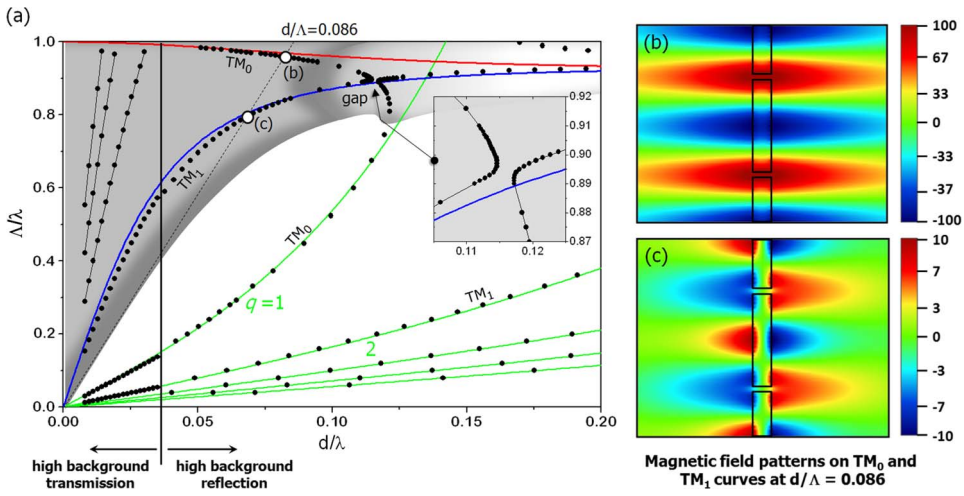

Fig. 4. Map of the SPP regime. (a) Dispersion map detailing purest SPP states and mode gap. Gray shading indicates the region with strong SPP character. Line color representations for coupled SPPs and CMs are the same as in Fig. 3(b). The inset shows a close-up of the crossing point between TM_0 and TM_1 curves. In (b) and (c), we show magnetic field distributions of excited surface waves for a grating with $d/\Lambda = 0.086$. (b) Even mode along curve TM_0. (c) Odd mode along curve TM_1.

where $k_0 = 2\pi/\lambda$. For all green curves, $\phi_R = 0.351\pi$ as this value gives the best fit. Excellent match between the green curves and those obtained by rigorous simulation in the frequency and thickness ranges $\Lambda/\lambda < \Lambda/\lambda_{SPR}$, and $d/\Lambda > 0.1$ confirms that FP resonance pertaining to a fundamental SG mode is the chief resonance mechanism responsible for EOT in this region. Thus, we use the term CM to designate a mode built by FP resonance of a fundamental SG mode. Note that λ_{SPR} is the SPP resonance wavelength on a single metal/air interface with $\varepsilon_{metal} = -5$. In the upper frequency range $(\Lambda/\lambda > \Lambda/\lambda_{SPR})$, all dispersion curves traverse abruptly from the green curves to the left showing strong correlation with dispersion curves for coupled SPP modes (red and blue curves). The upper part of the TM_0 curve approaches the even-coupled SPP dispersion (red) curve, while a part of the TM_1 curve, which appreciably deviates from the CM dispersion locus $(q = 1)$, lines up with the odd mode coupled-SPP dispersion (blue) curve. In other words, the TM_1 mode, which is an odd mode, degenerates into the SPP odd mode when the thickness becomes too small to support a CM. Note that the resonances on the far left arise via higher order $(m > 1)$ coupling between the incident wave and an SPP mode, as explained in Fig. 1(b). According to these identified resonance mechanisms, we divide the dispersion map of Fig. 3(a) into three regions, namely, a pure SPP region, a mixed SPP/CM region, and a CM region, as noted on the figure with approximate shaded areas of demarcation.

Discussing these regions in further detail, Fig. 4(a) shows an expanded view of the left-hand side of the dispersion map for the small thickness range. For the chosen material and fill factor, we approximate the effective medium dielectric constant of the metal film as $\varepsilon_{eff} \approx -7.143$. The transmittance of a homogeneous film with this dielectric constant is $T = 0.5$ when the thickness of the film is $d/\lambda \approx 0.037$. Therefore, when $d/\lambda < 0.037$, the metal film can be treated as being very thin, and most of the light energy will transmit through it; the resonances are identified as high-reflectance peaks in this case. For the same reason, when $d/\lambda > 0.037$, the extraordinary diffraction spots are identified as high-transmittance peaks.

The purest SPP states, namely those without a CM character, reside toward the left side and top corner on the dispersion plot in Fig. 4(a). We see that EOT loci closely follow SPP loci for the homogeneous-film approximation for $\sim d/\lambda < 0.1$. Both resonance peaks associated with normalized thickness $d/\Lambda = 0.086$ are in this region, as noted on Fig. 4. Fig. 4(b) and (c) present magnetic field profiles corresponding to these EOT spots; these bear great similarity to the even and odd SPP field distributions associated with a homogeneous metallic waveguide. In Fig. 4, color scales on the right indicate field-amplitude values that are normalized by the incident magnetic field

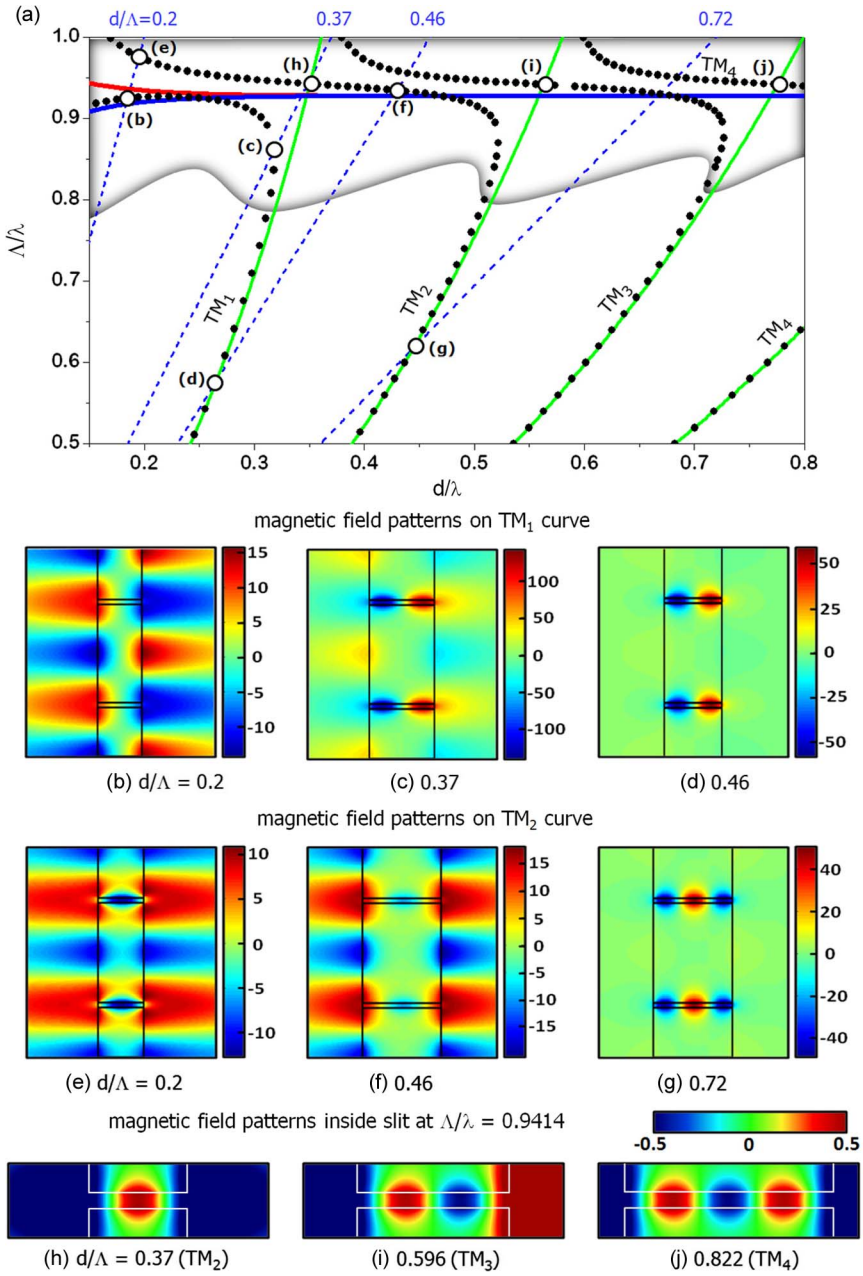

Fig. 5. Map of the SPP/CM regime. (a) Close-up of the dispersion map illustrating the mixed SPP and CM region at high frequency. Line color representations for coupled SPPs and CMs are the same as Fig. 3(b), and dots indicate EOT loci. (b)–(g) Comparison of magnetic field patterns along the TM_1 and TM_2 resonance curves. The field patterns are normalized by the incident field and captured at the moment when the fields reach maximum. (h)–(j) Comparison of magnetic field patterns on the TM_2, TM_3, and TM_4 EOT curves when the SPP excitation on the interface is maximized at $\Lambda/\lambda = 0.9414$ with fields normalized by the amplitude of the SPP field on the interface.

amplitude. The odd-symmetry resonance in Fig. 4(c) has a much smaller amplitude, meaning it has lower *Q* and larger linewidth consistent with the spectrum in Fig. 2(a). In these field plots, no CM signature appears.

A gap forms where the TM_0 and TM_1 EOT curves cross as shown in Fig. 4(a). The gap is a characteristic of the CM–SPP metamorphosis at small thickness where the TM_0 CM crosses over to

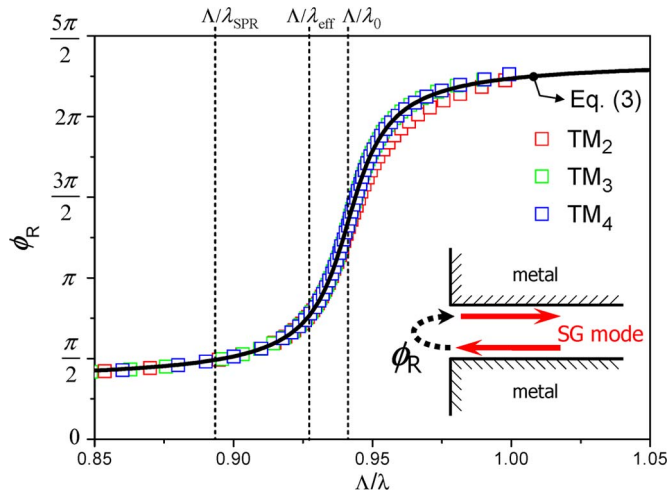

Fig. 6. Reflection phase of a fundamental SG mode in the SPP/CM region versus normalized frequency. Vertical dotted lines indicate resonance frequencies where λ_0 represents SPP resonance wavelength fitted to (3), λ_{eff} corresponds to the effective metal surface ($\varepsilon_{\text{metal}} = -7.143$), and λ_{SPR} pertains to the bare metal surface ($\varepsilon_{\text{metal}} = -5$). The best fit of (3) (black curve) to the inferred values (square symbols) is obtained with $\omega_0 = 0.9413 \times 2\pi c/\Lambda$ and $\gamma_{\text{rad}} = 0.01074 \times 2\pi c/\Lambda$, where c is the speed of light.

the even SPP and the TM_1 CM to the odd SPP, as required by symmetry. The local fields near the gap interfere and cancel the EOT, resulting in a reflectance peak instead.

Consider now $\sim d/\lambda > 0.2$ and the high-frequency part of the map ($\Lambda/\lambda > \Lambda/\lambda_{\text{SPR}}$) provided in Fig. 5(a). We will examine the local magnetic field amplitudes at points (b–j) marked thereon. The pattern in Fig. 5(b) shows a dominant SPP structure. Other representative field patterns exhibit coexisting SPPs and CMs, as in Fig. 5(e), (f), and (c). Fig. 5(c) shows the field profile at a lower frequency with the concentration of energy having gradually moved from the cover/substrate surface into the air slits; thus, we observe the appearance of the CM and fading of the SPP mode. As the frequency further decreases toward the CM region, the SPP features diminish, and the remaining CMs become the dominant resonance mechanism. This is clearly shown in Fig. 5(d) and (g) belonging to the CM region.

The dispersion map for thickness $\sim d/\lambda > 0.2$ reveals persistent FP characteristics in the mixed SPP/CM region. As shown in Fig. 3, the d/λ separation of the modal curves (TM_2 and higher resonances $i \geq 2$) in the SPP/CM region is $\sim$constant for a given frequency, even though they largely deviate from the FP resonances of the fundamental SG mode in an isolated slit denoted by the green curves in Fig. 3(b). Our computations show that the fundamental SG mode is strongly excited, even when the SPP mode on the interface becomes maximized at frequency $\Lambda/\lambda = 0.9414$. This is illustrated in Fig. 5(h)–(j), in which the fields are normalized by the SPP field on the external grating surface. The slit-mode structure is built by the CM/SPP combination yielding TM_2, TM_3, and TM_4 mode profiles as shown.

Finally, we explain further the transition characteristics of the modal curves. As shown in Figs. 3(b) and 5(a), the $TM_{i\geq 2}$ curves transition from the FP resonance locus for $q = i + 1$ to that for $q = i - 1$ while partly aligning with the SPP dispersion curves. For example, the TM_3 CM swings toward the SPP locus and then departs from it to join the TM_1 FP modal curve. Applying (1), the numerical mode spacing gives the propagation constant of an SG mode with ϕ_R eliminated, i.e., $\pi/\beta_{\text{SG}} = d_{q+1} - d_q$. We compare β_{SG} calculated by (2) with that thus estimated, and we find perfect agreement. Using (1) with the known value of β_{SG} from (2), ϕ_R can be inferred from the $TM_{i\geq 2}$ curves, as shown in Fig. 6. We hence attribute the modal transitions to the abrupt increase in ϕ_R when the surface of the metal film becomes resonant due to SPP excitation. The 2π phase shift shown supports the total transition—for example, the TM_3 to TM_1 transition.

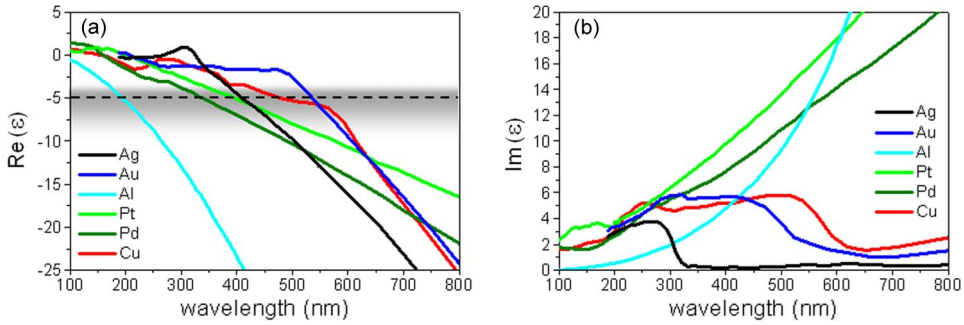

Fig. 7. Dispersion characteristics of example metals. (a) Re(ε) for Ag (black), Au (blue), Al (cyan), Pt (green), Pd (dark green), and Cu (red). The horizontal dashed line marks $\mathrm{Re}(\varepsilon) = -5$ with corresponding wavelengths being 409 nm (Ag), 534 nm (Au), 195 nm (Al), 394 nm (Pt), 338 nm (Pd), and 479 nm (Cu). (b) Corresponding Im(ε).

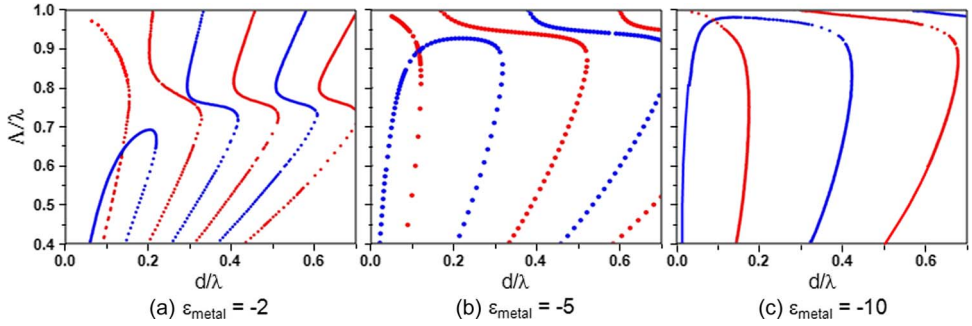

Fig. 8. Variation of the parametric map as Re(ε) changes.

The reflection phase bears resemblance to a typical phase behavior at the SPP resonance condition expressed as [24]–[26]

$$\phi_R = \phi_\infty - 2\tan^{-1}\left[\frac{\gamma_{\mathrm{rad}}}{(\omega - \omega_0)}\right] \tag{3}$$

where ω_0 is resonance frequency and γ_{rad} is the radiation rate of the SPP's decay into the reflected CM. The second term on the right-hand side of (3) describes the resonant phase change, and ϕ_∞ is the nonresonant reflection phase equal to 0.351π in our example.

3. Applicability of the Results

The study is limited by the restriction of a fixed dielectric constant. As real metals are highly dispersive, this limits the applicable spectral range to relatively narrow wavelength bands at which $\varepsilon_{\mathrm{metal}} \sim -5.0$. Fig. 7 shows the dispersion characteristic of several common metals. For example, for Ag, wavelengths near 400 nm pertain to $\varepsilon_{\mathrm{metal}} \sim -5.0$; the metals shown fall in the range of ~200–550 nm, as seen in Fig. 7(a). In Fig. 7(b), the dispersion of the imaginary part of the dielectric constant for each metal is shown. In this paper, we ignore effects of loss as it does not strongly affect the resonance loci but primarily reduces EOT efficiency. We note, however, that with loss, resonance peaks that are spectrally very narrow will disappear. We see that Ag at 400 nm has a relatively low loss at $\varepsilon_{\mathrm{metal}} \sim -5.0$. Fig. 8 shows how variation of the dielectric constant affects the EOT maps. The resonance loci shift, but the character and key features of the map persist. In the perfect electric conductor (PEC) approximation, where $\varepsilon_{\mathrm{metal}} \to -\infty$, we have $\lambda_{\mathrm{SPR}} = \Lambda[\varepsilon_{\mathrm{metal}}/(1+\varepsilon_{\mathrm{metal}})]^{1/2} \approx \Lambda$, and the curves push toward $\Lambda/\lambda = 1$, which is the

Rayleigh limit. Moreover, for PEC, (1) and (2) show that the lateral CM spacing becomes $(d_{q+1} - d_q)/\lambda = 0.5$. These trends are observable even in the case of $\varepsilon_{metal} = -10$.

The maps in Figs. 3–5 represent families of devices. To traverse the maps, on account of the fixed dielectric constant, we scan in normalized frequency Λ/λ by varying the period Λ rather than the wavelength λ. Similarly, we scan in normalized thickness d/λ by varying d directly. In this way, each resonance state on the maps can be reached, thereby aiding in device design.

4. Conclusion

In summary, through systematic numerical computations, we investigated the resonance properties of 1-D periodic metal slit arrays. By mapping the resonance loci, the modal and plasmonic mechanisms responsible for EOT emerge clearly with delineated regions of dominance. Computed magnetic field profiles at representative resonance loci define relative strengths of SPPs and CMs in the various regions. These results connect EOT resonances with pure SPP, coexisting SPP and CM, and pure CM, in general accordance with the published literature [1]–[15], [17], [18]. The map furthermore elucidates many interesting and novel physical properties of EOT resonance. For example, it shows how the TM_1 CM seamlessly morphs into the odd SPP mode as the film thickness diminishes. Similarly, the TM_0 mode converts to the even SPP mode. At the intersection of these mode curves, an EOT-free gap forms due to their interaction. On account of a reflection phase shift of an SG mode, an abrupt transition of the resonance loci in the SPP/CM region is observed. This approach, which can be extended to other model resonance systems, strengthens physical understanding of EOT and may aid in advancing associated applications.

References

[1] T. W. Ebbesen, H. J. Lezec, H. F. Ghaemi, T. Thio, and P. A. Wolff, "Extraordinary optical transmission through sub-wavelength hole arrays," *Nature*, vol. 391, pp. 667–669, Feb. 1998.

[2] F. J. Garćia-Vidal, L. Martin-Moreno, T. W. Ebbesen, and L. Kuipers, "Light passing through subwavelength apertures," *Rev. Mod. Phys.*, vol. 82, no. 1, pp. 729–787, Jan.–Mar. 2010.

[3] Y. Ding and R. Magnusson, "Resonant leaky-mode spectral-band engineering and device applications," *Opt. Express*, vol. 12, no. 23, pp. 5661–5674, Nov. 2004.

[4] R. Gordon, "Bethe's aperture theory for arrays," *Phys. Rev. A*, vol. 76, no. 5, pp. 053806-1–053806-5, Nov. 2007.

[5] L. Martín-Moreno, F. J. García-Vidal, H. J. Lezec, K. M. Pellerin, T. Thio, J. B. Pendry, and T. W. Ebbesen, "Theory of extraordinary optical transmission through subwavelength hole arrays," *Phys. Rev. Lett.*, vol. 86, no. 6, pp. 1114–1117, Feb. 2001.

[6] W. L. Barnes, W. A. Murray, J. Dintinger, E. Devaux, and T. W. Ebbesen, "Surface plasmon polaritons and their role in the enhanced transmission of light through periodic arrays of subwavelength holes in a metal film," *Phys. Rev. Lett.*, vol. 92, no. 10, pp. 107401-1–107401-4, Mar. 2004.

[7] H. Liu and P. Lalanne, "Microscopic theory of the extraordinary optical transmission," *Nature*, vol. 452, no. 7188, pp. 728–731, Apr. 2008.

[8] Q. Cao and P. Lalanne, "Negative role of surface plasmons in the transmission of metallic gratings with very narrow slits," *Phys. Rev. Lett.*, vol. 88, no. 5, pp. 057403-1–057403-4, Jan. 2002.

[9] G. Gay, O. Alloschery, B. Viaris de Lesegno, C. O'Dwyer, J. Weiner, and H. J. Lezec, "The optical response of nanostructured surfaces and the composite diffracted evanescent wave model," *Nature Phys.*, vol. 2, pp. 262–267, Apr. 2006.

[10] J. Weiner, "The physics of light transmission through subwavelength apertures and aperture arrays," *Rep. Prog. Phys.*, vol. 72, no. 6, pp. 1–19, May 2009.

[11] Y. Xie, A. R. Zakharian, J. V. Moloney, and M. Mansuripur, "Transmission of light through a periodic array of slits in a thick metallic film," *Opt. Express*, vol. 13, no. 12, pp. 4485–4491, Jun. 2005.

[12] Y. Pang, C. Genet, and T. W. Ebbesen, "Optical transmission through subwavelength slit apertures in metallic films," *Opt. Commun.*, vol. 280, no. 1, pp. 10–15, Dec. 2007.

[13] J. A. Porto, F. J. García-Vidal, and J. B. Pendry, "Transmission resonances on metallic gratings with very narrow slits," *Phys. Rev. Lett.*, vol. 83, no. 14, pp. 2845–2848, Oct. 1999.

[14] F. Marquier, J. Greffet, S. Colin, F. Pardo, and J. Pelouard, "Resonant transmission through a metallic film due to coupled modes," *Opt. Express*, vol. 13, no. 1, pp. 70–76, Jan. 2005.

[15] D. Crouse and P. Keshavareddy, "Role of optical and surface plasmon modes in enhanced transmission and applications," *Opt. Express*, vol. 13, no. 20, pp. 7760–7771, Oct. 2005.

[16] T. K. Gaylord and M. G. Moharam, "Analysis and applications of optical diffraction by gratings," *Proc. IEEE*, vol. 73, no. 5, pp. 894–937, May 1985.

[17] M. M. Treacy, "Dynamical diffraction explanation of the anomalous transmission of light through metallic gratings," *Phys. Rev. B, Condens. Matter*, vol. 66, no. 19, pp. 195105-1–195105-11, Nov. 2002.

[18] B. Sturman, E. Podivilov, and M. Gorkunov, "Theory of extraordinary light transmission through arrays of subwavelength slits," *Phys. Rev. B, Condens. Matter*, vol. 77, no. 7, pp. 075106-1–075106-12, Feb. 2008.
[19] J. J. Burke, G. I. Stegeman, and T. Tamir, "Surface-polariton-like waves guided by thin, lossy metal films," *Phys. Rev. B, Condens. Matter*, vol. 33, no. 8, pp. 5186–5201, Apr. 1986.
[20] Y. Ding, "Resonant leaky-mode spectral-band engineering and device applications," Ph.D. dissertation, Dept. Elect. Eng., Univ. Connecticut, Storrs, CT, 2006.
[21] X. Jiao, P. Wang, L. Tang, Y. Lu, Q. Li, D. Zhang, P. Yao, H. Ming, and J. Xie, "Fabry–Pérot-like phenomenon in the surface plasmons resonant transmission of metallic gratings with very narrow slits," *Appl. Phys. B*, vol. 80, no. 3, pp. 301–305, Mar. 2005.
[22] T. Takakura, "Optical resonance in a narrow slit in a thick metallic screen," *Phys. Rev. Lett.*, vol. 86, no. 24, pp. 5601–5603, Jun. 2001.
[23] J. A. Dionne, L. A. Sweatlock, and H. A. Atwater, "Plasmon slot waveguide: Towards chip-scale propagation with subwavelength-scale localization," *Phys. Rev. B, Condens. Matter*, vol. 73, no. 3, pp. 035407-1–035407-9, Jan. 2006.
[24] K. Kurihara and K. Suzuki, "Theoretical understanding of an absorption-based surface plasmon resonance sensor based on Kretchmann's theory," *Anal. Chem.*, vol. 74, no. 3, pp. 696–701, Feb. 2002.
[25] H. Raether, *Surface Plasmons on Smooth and Rough Surfaces and on Gratings*. Berlin, Germany: Springer-Verlag, 1988.
[26] H. A. Haus, *Waves and Fields in Optoelectronics*. Englewood Cliffs, NJ: Prentice-Hall, 1984.